# Microconfined equiviscous droplet deformation : comparison of experimental and numerical results

# Microconfined equiviscous droplet deformation: Comparison of experimental and numerical results

Anja Vananroye,[1] Pieter J. A. Janssen,[2] Patrick D. Anderson,[2] Peter Van Puyvelde,[1] and Paula Moldenaers[1]
[1]*Department of Chemical Engineering, K. U. Leuven, W. de Croylaan 46, B-3001 Leuven, Belgium*
[2]*Materials Technology, Dutch Polymer Institute, Eindhoven University of Technology, P.O. Box 513, 5600 MB Eindhoven, Netherlands*

(Received 18 December 2006; accepted 3 December 2007; published online 29 January 2008)

The dynamics of confined droplets in shear flow is investigated using computational and experimental techniques for a viscosity ratio of unity. Numerical calculations, using a boundary integral method (BIM) in which the Green's functions are modified to include wall effects, are quantitatively compared with the results of confined droplet experiments performed in a counter-rotating parallel plate device. For a viscosity ratio of unity, it is experimentally seen that confinement induces a sigmoidal droplet shape during shear flow. Contrary to other models, this modified BIM model is capable of predicting the correct droplet shape during startup and steady state. The model also predicts an increase in droplet deformation and more orientation toward the flow direction with increasing degree of confinement, which is all experimentally confirmed. For highly confined droplets, oscillatory behavior is seen upon startup of flow, characterized by an overshoot in droplet length followed by droplet retraction. Finally, in the case of a viscosity ratio of unity, a minor effect of confinement on the critical capillary number is observed both numerically and experimentally. © *2008 American Institute of Physics*. [DOI: 10.1063/1.2835312]

## I. INTRODUCTION

In the past, a great deal of effort has been devoted to understanding the behavior of single droplets dispersed in a matrix fluid. The rheology and the dynamics of a Newtonian droplet surrounded by an immiscible Newtonian liquid are therefore well known. In this specific case, the droplet behavior in a shear flow field is determined by two nondimensional parameters: the capillary number Ca $(=\mu_m R\dot{\gamma}/\sigma$, where $\mu_m$, $R$, $\dot{\gamma}$, and $\sigma$ denote, respectively, the matrix viscosity, the droplet radius, the shear rate, and the interfacial tension), and the viscosity ratio $\lambda$ $(=\mu_d/\mu_m$, in which $\mu_d$ is the droplet viscosity). Upon startup of shear flow, an initially spherical droplet in an unbounded flow field deforms and orients monotonically until a steady-state shape and orientation is reached. The magnitude of the deformation increases with increasing Ca, and droplet breakup only occurs above a critical value $\mathrm{Ca}_{\mathrm{crit}}$.[1] Since the pioneering research of Taylor,[2] many theoretical and numerical studies describing the Newtonian droplet behavior in bulk flow have been developed and reviewed, showing all good agreement with experimental results.[3–6]

In the past decade, the use of microfluidic devices and applications in processing industries has grown to a large extent.[7,8] Many of these applications consider multiphase systems, for instance, to create dispersions with a desired droplet-size distribution.[9–12] Processing droplet-matrix systems on a microscale, where the droplet diameter is typically in the order of the channel height, largely affects the droplet behavior, since droplet-wall interactions come into play.[13] Some interesting studies on the behavior of blends and single droplets undergoing confined shear flow have already been performed.[14–20] For instance, the existence of superstructures such as pearl necklaces, strings, and single layers was demonstrated for blends with $\lambda=1$.[14–16] Similar patterns were found when shearing confined blends with $\lambda<1$.[17] For droplets in dilute emulsions, it was shown that bulk theories remained valid as long as the ratio of droplet size to gap spacing was below a critical confinement ratio.[17] Also the effect of confinement on the breakup conditions in shear flow has been investigated for several viscosity ratios.[18] For $\lambda$ near unity, no significant change in $\mathrm{Ca}_{\mathrm{crit}}$ was seen. However, when $\lambda<1$, confinement suppressed breakup, whereas for $\lambda>1$, breakup was enhanced.[18] Even highly viscous droplets in a confined emulsion with $\lambda>4$ could be broken easily, simply by applying a shear flow. It was reported that highly confined droplets displayed larger deformation and more orientation toward the flow direction than nonconfined ones during steady-state shear flow.[15,19,20] Not only an increase in the magnitude of the deformation, but also a change in the droplet shape was seen.[19,20] However, these recent observations all lack a good theoretical explication. Only a few studies were conducted including the effects of two parallel walls on the behavior of single droplets.[21–24] For instance, using an integral solution, Shapira and Haber calculated a first-order correction for wall effects that took into account the deviation from sphericity and the drag force acting upon a droplet in confined shear flow.[21] It was shown for equal viscosities that the obtained deformation parameter matched experimental results quite well.[19] Also for viscosity ratios unequal to 1, it was reported that this model is capable of predicting the effects of confinement on the deformation parameter.[20] However, the model predicts only a change in the deformation magnitude and not in the droplet shape, which contradicts

 

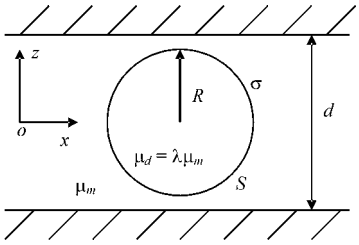


FIG. 1. Schematic representation of a droplet in a matrix fluid confined between two parallel plates located at $z=\pm W$ ($W=d/2$).

the experimental observations. Recently, for a viscosity ratio of 1, numerical simulations were developed to study droplet behavior in confined flows.[22–24] For instance, a boundary integral method (BIM) was used to study the behavior of a single droplet confined between two parallel walls.[23] The inclusion of wall effects in a boundary integral method was done by modification of the Green's functions.[23,25,26] This way, it is possible to predict the shape, dimensions, and orientation of confined droplets in shear flow for all viscosity ratios.

In this study, the experimentally determined behavior of confined single droplets is compared to the predictions of the modified BIM model for a viscosity ratio of unity. The shape, deformation, and orientation of droplets during startup and steady-state shear flow are considered. In addition, breakup is considered. Steady-state velocity and pressure profiles are calculated for unconfined and confined droplets in order to shed light on the underlying deformation mechanism.

## II. NUMERICAL PROCEDURE

### A. Mathematical formulation

The system is modeled as a Newtonian drop in a Newtonian matrix fluid under creeping flow conditions. In this limiting case, the interface velocity can be calculated with a boundary integral method.[27,28] Boundary integral methods have been used successfully to study drop dynamics in bulk flow conditions[29–33] or the movement of solid spheres and more recently drops between parallel walls.[34–36] In the boundary integral formulation, the velocity $\mathbf{u}$ at a point $\mathbf{x}_0$ on the interface is given by

$$(\lambda+1)\mathbf{u}(\mathbf{x}_0) = 2\mathbf{u}_\infty(\mathbf{x}_0) - \frac{1}{4\pi}\int_S \mathbf{f}(\mathbf{x})\cdot\mathbf{G}(\mathbf{x},\mathbf{x}_0)dS(\mathbf{x}) - \frac{\lambda-1}{4\pi}\int_S \mathbf{u}(\mathbf{x})\cdot\mathbf{T}(\mathbf{x},\mathbf{x}_0)\cdot\mathbf{n}(\mathbf{x})dS(\mathbf{x}), \quad (1)$$

where the integration is performed over all the fluid surfaces $S$ (see Fig. 1). Here, all lengths are scaled with $R$, time with $\dot{\gamma}$, velocities with $\dot{\gamma}R$, and pressures with $\sigma/R$. Furthermore, $\mathbf{G}$ and $\mathbf{T}$ are the Green's functions associated with a point force for velocity and stress, respectively, $\mathbf{n}$ is the normal vector to the interface, and $\mathbf{u}_\infty$ is the prescribed flow field. The kinematic condition at the interface is

$$\frac{d\mathbf{x}}{dt} = \mathbf{u}(\mathbf{x},t). \quad (2)$$

Since this study is limited to cases with viscosity ratio $\lambda$ of unity, the second integral on the right-hand side drops out. The Green's function $\mathbf{G}$ consists of a free-space part $\mathbf{G}^\infty$ and an additional contribution $\mathbf{G}^{2W}$ that corrects for the presence of the walls.[25,26] Griggs *et al.*[24] show that two single-wall reflection Green's functions perform very well as an approximation for the Green's function in Poiseuille flow as results obtained with this approximation compare very well with those from a full correct Green's function and from a Taylor expansion of these. Computation times for the flows considered in the current work were very acceptable using the method of Janssen and Anderson,[23] hence no efforts were invested to reduce computational costs using this approximation.

In Eq. (1), $\mathbf{f}$ is the discontinuity in the interfacial surface force, given by

$$\mathbf{f}(\mathbf{x}) = \frac{2}{\mathrm{Ca}}\kappa(\mathbf{x})\mathbf{n}(\mathbf{x}), \quad (3)$$

with $\kappa$ the local curvature, defined as $\kappa=\frac{1}{2}\nabla_s\cdot\mathbf{n}$, where $\nabla_s$ is the surface gradient operator: $\nabla_s=(\mathbf{I}-\mathbf{nn})\cdot\nabla$. Similar to the velocity, the pressure $p$ outside the drop, scaled with $\sigma/R$, can also be expressed as a boundary integral.[28] For drops with $\lambda=1$, this expression is

$$p(\mathbf{x}_0) = -\frac{\mathrm{Ca}}{8\pi}\int_S \mathbf{f}(\mathbf{x})\cdot\mathbf{Q}(\mathbf{x}_0,\mathbf{x})\mathrm{d}S(\mathbf{x}). \quad (4)$$

Here, $\mathbf{Q}(\mathbf{x},\mathbf{x}_0)$ is the pressure vector associated with the Green's function $\mathbf{G}(\mathbf{x},\mathbf{x}_0)$. Similar to the Green's function for the velocity, the pressure vector also consists of a free-space part and a contribution due to the presence of the walls,

$$\mathbf{Q} = \mathbf{Q}^\infty + \mathbf{Q}^{2W}, \quad (5)$$

where $\mathbf{Q}^\infty$ is given by

$$\mathbf{Q}^\infty(\mathbf{x},\mathbf{x}_0) = 2\frac{\hat{\mathbf{x}}}{|\hat{\mathbf{x}}|^3}, \quad (6)$$

with $\hat{\mathbf{x}}=\mathbf{x}-\mathbf{x}_0$. The wall contribution $\mathbf{Q}^{2W}$ is expressed, assuming the walls are located at $z\pm W$, in a similar matter as $\mathbf{G}^{2W}$,[23,25]

$$Q_x^{2W}(\mathbf{x},\mathbf{x}_0) = 2\frac{\hat{x}}{s}\int_0^\infty qJ_1(qs)p_{1p}\mathrm{d}q, \quad (7)$$

$$Q_z^{2W}(\mathbf{x},\mathbf{x}_0) = 2\int_0^\infty qJ_0(qs)p_{1n}\mathrm{d}q, \quad (8)$$

with $s=\sqrt{\hat{x}^2+\hat{y}^2}$, and $Q_y^{2W}$ is the same as $Q_x^{2W}$ with $\hat{x}$ replaced by $\hat{y}$. The integrands are derived from Jones[25] and are given by

$$p_{1p} = E_-[A_-\cosh(v) - v\sinh(v)]\cosh(w) + E_+[B_-\sinh(v) - v\cosh(v)]\sinh(w), \quad (9)$$

$$p_{1n} = E_-[B_+ \sinh(v) - v\cosh(v)]\cosh(w) + E_+[A_+ \cosh(v) - v\sinh(v)]\sinh(w), \quad (10)$$

where $A_\pm$, $B_\pm$, and $E_\pm$ are functions of $qW$.[23,25] Furthermore, $v=qz_0$, $w=qz$, and $J_\nu$ is a Bessel function of the first kind with order $\nu$. Similar to the Green's functions for the velocity, the integration over $q$ is done by converting the integrals into a fast decaying part, which is handled numerically, and a slow decaying part, which is handled analytically,[23,34]

$$Q_z^{2W} \approx 2\int_0^{\xi} qJ_0(p_{1n} - \breve{p}_{1n})dq + 2\int_0^{\infty} qJ_0(qs)\breve{p}_{1n}(q,z,z_0)dq, \quad (11)$$

with $\xi=7$. The fast decaying terms for the pressure vector are

$$\breve{p}_{1n} = [\{2(W-z_0)\}q+1]\exp([z+z_0-2W]q) - [\{2(W+z_0)\}q+1]\exp([-z-z_0-2W]q), \quad (12)$$

$$\breve{p}_{1p} = [\{2(W-z_0)\}q-1]\exp([z+z_0-2W]q) + [\{2(W+z_0)\}q-1]\exp([-z-z_0-2W]q). \quad (13)$$

Details of the numerical evaluation of these integrals can be found elsewhere.[23] Observe that for a correct implementation in Eq. (4), $\mathbf{x}$ and $\mathbf{x}_0$ in Eqs. (6)–(8) have to be switched.

The pressure field is calculated by defining a rectangular grid around the drop and in each point Eq. (4) is evaluated. A simple near-singular subtraction technique is used to handle the singularity of $\mathbf{Q}^\infty$ as $\mathbf{x}$ approaches $\mathbf{x}_0$,

$$p(\mathbf{x}_0) = -\frac{\mathrm{Ca}}{8\pi}\int_S [\mathbf{f}(\mathbf{x}) - \mathbf{f}(\mathbf{x}^*)]\cdot\mathbf{Q}(\mathbf{x}_0,\mathbf{x})\mathrm{d}S(\mathbf{x}) + cf_n(\mathbf{x}^*), \quad (14)$$

with $\mathbf{x}^*$ the location of the closest node on the drop surface, $f_n=\mathbf{f}\cdot\mathbf{n}$, and $c$ is a constant, which is 0 when $\mathbf{x}_0$ is outside and $8\pi$ when $\mathbf{x}_0$ is inside the drop.

### B. Numerical implementation

The singularity of the free-space kernel $\mathbf{G}$ is handled via a nonsingular contour integration.[37] Details concerning the implementation of the wall contribution to $\mathbf{G}$ can be found elsewhere.[23] A standard contour integration is used for the curvature calculation.[38] The mesh is generated from a regular icosahedron, of which each triangular surface element is subdivided into 20 smaller triangles, yielding 8000 elements (4002 nodes) in total. No remeshing is performed during a simulation. The normal component of the velocity, calculated with Eq. (1), is used to update the position of the interface. In addition, nodes are advected with an additional tangential velocity that moves nodes to places with high curvature.[38] To limit computation time, a multitime step algorithm is used,[37] in which the kernels are only calculated every 50 time steps. A time step of $5\times10^{-4}$ is used in all cases. The maximum distance between two points on the drop interface, and the orientation angle, are calculated by fitting a local paraboloid.[30] All details concerning the implementation and the convergence of the results as a function of the number of nodes can be found in Janssen and Anderson.[23]

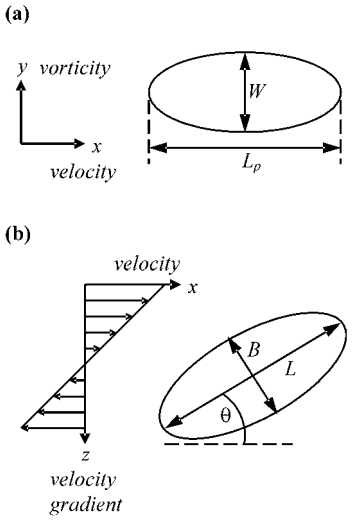


FIG. 2. Schematic representation of a deformed droplet with the geometrical parameters in shear flow: (a) Velocity-vorticity plane; (b) velocity-velocity gradient plane.

## III. EXPERIMENTAL PROCEDURE

The experiments are performed in a counter-rotating parallel plate device (Paar-Physica). This type of flow cell has the advantage that a droplet can be held in a stagnation plane during shear flow without any time or distance limits. A detailed description of the device is given elsewhere.[18] All experiments are performed in a thermostatic room at room temperature. The gap between the plates is kept constant at 1 mm, and is filled with the continuous phase. The degree of confinement, defined as the ratio of droplet diameter $2R$ to gap spacing $d$ (see Fig. 1), is varied by carefully injecting isolated droplets with different sizes using a homemade injection system. Droplets that are not positioned in the center plane between the plates are excluded from the experiment. The visualization of droplets occurs in the velocity-vorticity plane as well as in the velocity-velocity gradient plane. During startup of shear flow, images are first captured in the vorticity-velocity plane, as shown in Fig. 2(a), until the steady-state regime is reached. Then the flow is stopped, and after relaxation of the droplet the same experiment is performed while capturing images in the velocity-velocity gradient plane, as shown in Fig. 2(b). This way, it is possible to extract all information about the dynamics of the droplets during flow.

As the continuous phase, a poly(isobutylene) liquid (PIB, Parapol 1300 from ExxonMobil Chemical, USA) is used. The droplet phase consists of a poly(dimethyl siloxane) liquid (PDMS 100000, Rhodorsil from Rhodia Chemicals, France). Both pure materials exhibit a fairly Newtonian behavior with constant viscosities up to the highest shear rates used in the experiments. As elasticity effects are negligible, the components behave as Newtonian fluids under the measurement conditions.[39] The viscosities $\mu_m$ and $\mu_d$ of PIB and PDMS, respectively, are 103.8 and 103.7 Pa s at 23.7 °C, resulting in a viscosity ratio $\lambda$ close to 1 at room temperature. The interfacial tension $\sigma$ of the PDMS/PIB system is

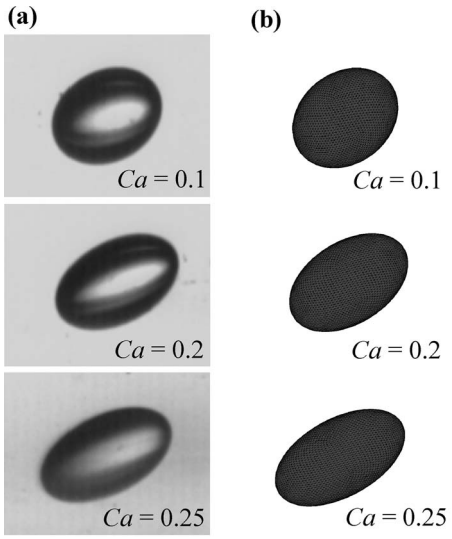


FIG. 3. Steady-state droplet shape in the velocity-velocity gradient plane at Ca=0.1, 0.2, and 0.25 for $2R/d=0.18$: (a) Experimental data and (b) numerical data.

reported to be 2.8 mN/m.[40] The difference in density between PIB ($\rho_{PIB}=890$ kg/m$^3$ at 20 °C) and PDMS ($\rho_{PDMS}=970$ kg/m$^3$ at 20 °C) is small enough to neglect gravitational effects.[41]

## IV. RESULTS AND DISCUSSION

### A. Steady state

Figure 3 shows the steady-state shapes of a droplet with a degree of confinement of 0.18 at different capillary numbers. For $2R/d<0.2$, it was reported that wall effects are still negligible and bulk flow still prevails.[20] In Fig. 3(a), the experimentally observed shapes recorded in the velocity-velocity gradient plane are depicted. The corresponding shapes calculated from the numerical simulations are shown in Fig. 3(b). As can be seen, a good agreement between the numerical plots and the experimental images is present for all three capillary numbers shown here. Both series of images display an ellipsoidal droplet shape for all Ca, as can be expected for nonconfined droplets. Note that the experimental images taken in the velocity-velocity gradient direction (as in Figs. 3 and 5) are slightly optically deformed in the velocity direction due to the cylindrical curvature of the glass cup surrounding the plates. Therefore, a spherical droplet is weakly seen as an elliptical one with its longest axis in the velocity direction. Consequently, the visualization of deformed droplets also suffers from this aberration, and hence a larger droplet orientation toward the flow direction than actually present is microscopically seen. However, the image analysis procedure used for this type of experiment only takes into account correctly visualized dimensions of the droplets, hence the main axes $L$ and $B$ of the droplet in the velocity-velocity gradient plane are not directly obtained from the images but calculated using the correctly represented dimensions. The images show a decrease in orientation angle $\theta$ [see Fig. 2(b)] and thus more orientation toward the flow direction, with increasing capillary number. At first glance, it can be concluded that the numerical BIM model with integrated wall effects is capable of predicting the shape of droplets under bulk flow conditions.

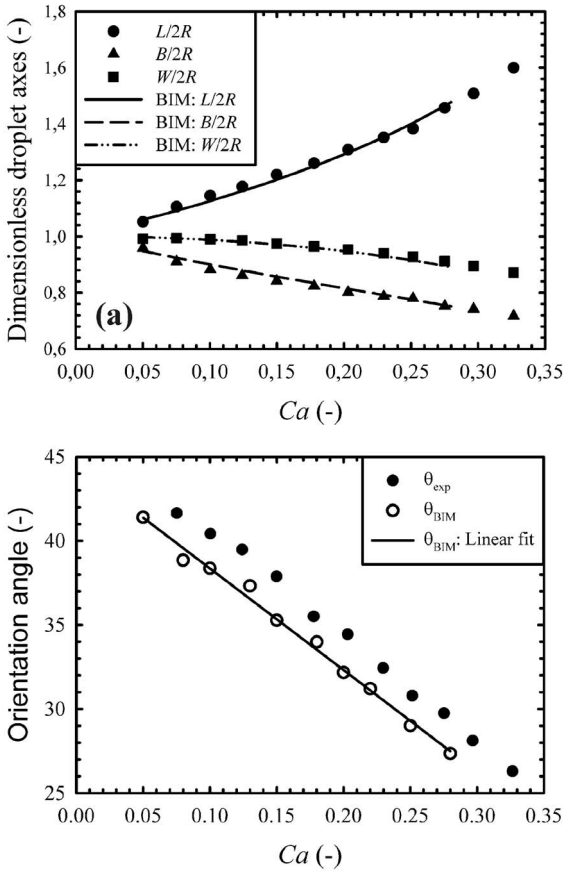


FIG. 4. Comparison between experimental data and numerical simulations for $2R/d=0.18$ as a function of capillary number: (a) Dimensionless droplet axes and (b) orientation angle.

To quantify the previous results, the dimensionless axes [Fig. 4(a)] and the orientation angle [Fig. 4(b)] of the nonconfined droplet are shown as a function of Ca. The lines in the graphs represent the dimensionless axes and orientation angle calculated from the modified BIM model. As can be seen in Fig. 4(a), the model is perfectly capable of predicting the main axes $L/2R$, $B/2R$, and $W/2R$ (see Fig. 2) of the droplet during steady-state shear flow up to capillary numbers not far from the critical value. The prediction of the orientation angle $\theta$, however, is slightly different from the experimental results. The model predicts more orientation toward the flow direction than experimentally observed. Despite these small deviations, the modified BIM model predicts quite accurately the trend in orientation angle with increasing Ca. Therefore, it can be concluded that the model is able to give the full three-dimensional steady-state shape and dimensions of an unconfined deformed droplet up to capillary numbers of 0.4. The model is also capable of predicting the decreasing trend in orientation angle as a function of Ca.

In Fig. 5, the experimentally determined steady-state shapes of a confined droplet ($2R/d=0.82$) and the numerically determined steady-state shapes at the same confinement ratio are shown for three different capillary numbers. When

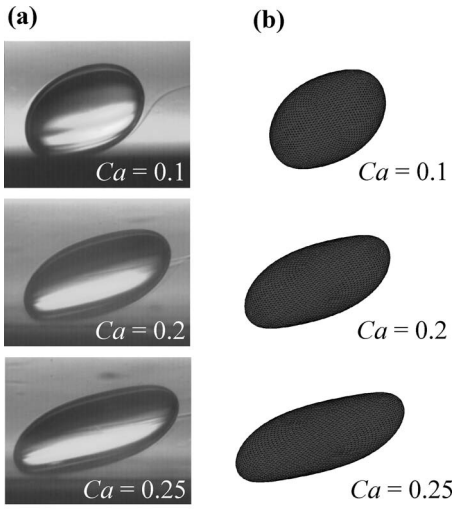


FIG. 5. Steady-state droplet shape in the velocity-velocity gradient plane at Ca=0.1, 0.2, and 0.25 for $2R/d=0.83$: (a) Experimental data and (b) numerical data.

comparing the experimental images of this confined droplet [Fig. 5(a)] with the experimental images of the unconfined droplet [Fig. 3(a)], it is immediately clear that confinement affects the deformation of a droplet at a constant Ca. It is seen that not only the magnitude of the deformation, but also the shape of the deformed droplet is changed due to the proximity of the walls. Instead of an ellipsoid, which is the characteristic shape for droplets in a bulk shear flow, a sigmoidal deformation with slightly more pronounced pointed ends is present in a confined shear flow. The results of the numerical model [Fig. 5(b)] display great similarity with the experimental droplet shape [Fig. 5(a)] for all three capillary numbers under investigation. Contrary to the model of Shapira and Haber,[21] this model predicts both a change in shape and an increase in deformation magnitude. Therefore, it can be stated that this model is capable of describing the steady-state shape of confined droplets in any shear flow field.

Figure 6 shows the dimensionless axes [Fig. 6(a)] and the orientation angle [Fig. 6(b)] as a function of *Ca* for this confined droplet. The lines represent the results calculated from the simulations for $\lambda=1$ and $2R/d=0.83$. Both the experimental results and the model calculations for the confined droplet show large differences with respect to the limiting bulk behavior (see Fig. 4). Clearly a larger distortion from the spherical shape is present due to the confining effect of the walls. The experimental and the numerical results of the confined droplet are in good agreement. All three main axes of the droplet and its orientation in the flow field are reproduced nicely by the model. The model is, therefore, not only capable of predicting the right shape, as stated before, but also the deformation magnitude and orientation angle match nicely the experimental results up to capillary numbers around 0.3.

In order to explain the observed results, the velocity and pressure profiles in and around the droplet are calculated. In Fig. 7, numerically obtained velocity profiles are given in the $y=0$ plane at a capillary number of 0.25 for an unconfined

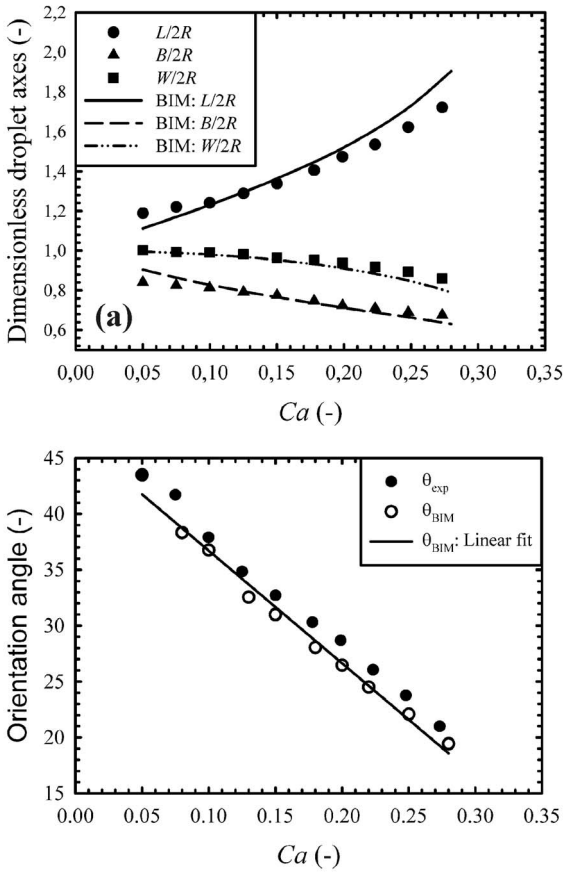


FIG. 6. Comparison between experimental data and numerical simulations for $2R/d=0.83$ as a function of capillary number: (a) Dimensionless droplet axes and (b) orientation angle.

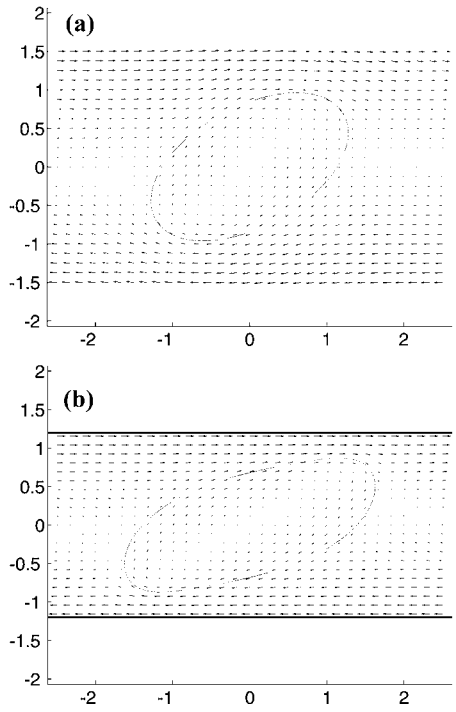


FIG. 7. Velocity profiles for Ca=0.25: (a) $2R/d=0$ and (b) $2R/d=0.83$.

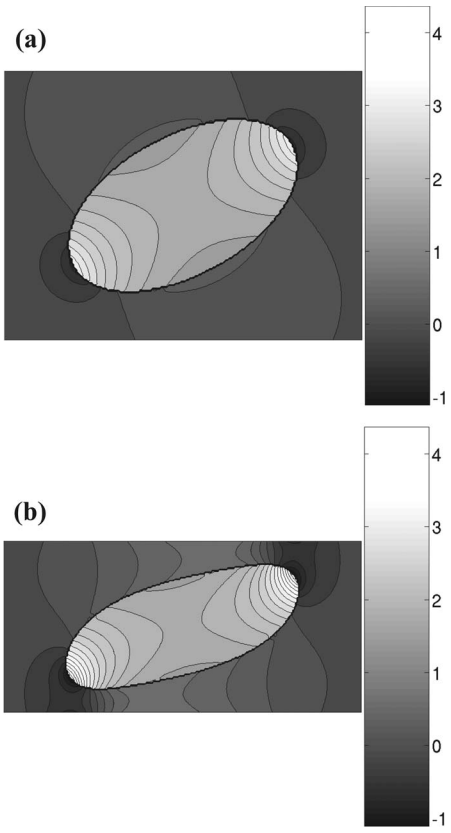


FIG. 8. Pressure distribution for Ca=0.25: (a) $2R/d=0$ and (b) $2R/d=0.83$.

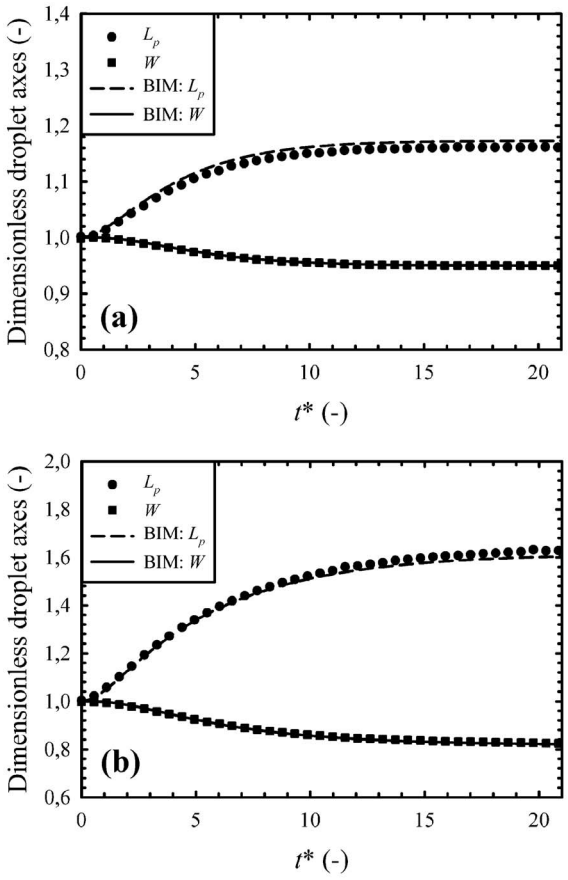


FIG. 9. Comparison between experimental startup data and numerical simulations for $2R/d=0.19$ as a function of dimensionless time: (a) Ca=0.2 and (b) Ca=0.35.

[Fig. 7(a)] and a confined [Fig. 7(b)] droplet. In both cases, the velocities inside the droplet follow the same recirculation pattern. The resulting streamlines are closed and no dead zones can be observed, not even in the case of confined droplets. Hence at $\lambda=1$, the velocity profile inside the droplet does not seem to influence the deformation behavior between the confined and unconfined case. Outside the drop, the gap between the wall and the droplet surface is extremely narrow near the ends of the drop, leading to an increased shear rate in the matrix fluid at those places. As a consequence, the shape of a confined droplet is changed from ellipsoidal to sigmoidal and the deformation is increased. Similar findings were reported by Renardy.[22]

Next, we present pressure profiles in the $y=0$ plane obtained from the simulations. For the drop in bulk conditions [Fig. 8(a)], high pressures are found on the inside of the drop near the tips, where the curvature of the interface is high. On the other hand, near regions with low curvature, like the waist of the drop, the pressure is even lower than the resulting pressure in a spherical drop, which is $2\sigma/R$, or 2 in our scaled variables. Just outside the drop we find a pressure lower than 0 near the tips and higher than 0 near places with low curvature. However, the case for the confined drop is significantly different, as can be seen in Fig. 8(b). Near the tips we find an even higher pressure than the drop in bulk flow conditions. As the curvature here is also larger, this is to be expected. Once again, we find lower pressure inside the drop near places with low curvature. The main difference, however, is outside the drop. The wedge that forms between the drop and the wall leads to a large increase of the pressure. In fact, the pressure approaches values as high as 1 in those areas. Subsequently, the pressure drop behind the wedge is huge, as also there the pressure is lower due to the high curvature. It is believed that this changed pressure profile is responsible for the changed droplet dynamics, although no conclusive statement can be made at present. In order to investigate this effect more systematically, a comparison between simulations and experiments at different viscosity ratios is necessary since it is known that the viscosity ratio drastically affects the droplet dynamics in confinement.

### B. Startup

Next to the steady-state behavior, also the transient droplet behavior during startup of shear flow is investigated. In Fig. 9(a), the transient shape during startup of shear flow is shown for an unconfined droplet ($2R/d=0.19$), at a capillary number of 0.2. The deformation is expressed as a function of the dimensionless time $t^*$ ($t^*=t/\tau$ with $t$ the absolute time and $\tau=\mu_m R/\sigma$ a characteristic emulsion time). The dimensionless projections of the droplet in the vorticity-velocity plane, namely $L_p/2R$ and $W/2R$ (see Fig. 2), will be used here to express the deformation of the droplets. This way, no

further shape calculations have to be performed on the images obtained during the experiments and no numerical calculations of the orientation angle have to be performed. The lines in Fig. 9 represent the corresponding predictions of the model. For $\lambda=1$, the numerical model is capable of predicting the shape evolution of the confined droplet during startup of flow. At every point in time, the model corresponds well with the experimental data. It is seen that the shape of the droplet during startup remains ellipsoidal at all times. The magnitude of the deformation of the ellipsoidal droplet changes monotonically with time until steady state is reached, as is exactly the case for nonconfined droplets. Both the model and the experimental results reach the steady-state shape at the same moment in time. In Fig. 9(b), comparable results for the same droplet, yet at a more elevated capillary number of 0.35, are shown. Also here, good agreement between experimental results and the numerical simulations is present. Therefore, it can be concluded that the numerical model is capable of predicting the transient startup dynamics in shear flow in the limiting case of a nonconfined droplet.

The results for a confined droplet during startup of flow at a capillary number of 0.2 are illustrated in Fig. 10. In Fig. 10(a), it can be seen that the model (lines in the graph) predicts a large overshoot in $L_p/2R$, which occurs simultaneously with an undershoot in $W/2R$. Similar observations are experimentally obtained. However, the overshoot in $L_p/2R$ is less pronounced and less deformation is seen at the final steady state. Both experimental and numerical results indicate that a confined droplet does not deform monotonically toward its steady-state shape but passes first through a maximum in deformation before retracting to its steady-state deformation. The steady-state regime also settles in at a later point in time compared to the unconfined situation. In Figs. 10(b) and 10(c), the shape evolution during startup is both numerically and experimentally shown. As can be seen on the microscopic images, the droplet displays a sigmoidal shape already immediately after startup. This is also predicted by the numerical simulation, and again good agreement between the experimental and numerical images is seen. Since the shape of the droplet is sigmoidal, no unique definition of the orientation angle can be given. Therefore, the angle is not experimentally determined or calculated and only the projections are used to quantify the droplet shape.

In Fig. 11, the droplet shape is shown as a function of time for a confined droplet at a capillary number of 0.35. As can be seen in Fig. 11(a), both the experimental results and the predictions of the numerical model show a large overshoot in $L_p$. This overshoot occurs at a time scale in which steady state has already been reached normally in bulk flow. Although the experimental maximum occurs a little bit later in time, good agreement between the experimental droplet length and the numerically calculated length is seen. In the experimental and numerical images in Figs. 11(b) and 11(c), a very elongated, sigmoidal droplet is seen. Again, the sigmoidal shape is present from the beginning of startup. At the maximal deformation, the center part of the body shows some slight necking, although no breakup is seen. Instead, the droplet retracts to its sigmoidal steady-state deformation. The model calculations and shapes show an excellent similarity with the experimental observations. Good agreement is present for low and high capillary numbers and for both confined and unconfined droplets.

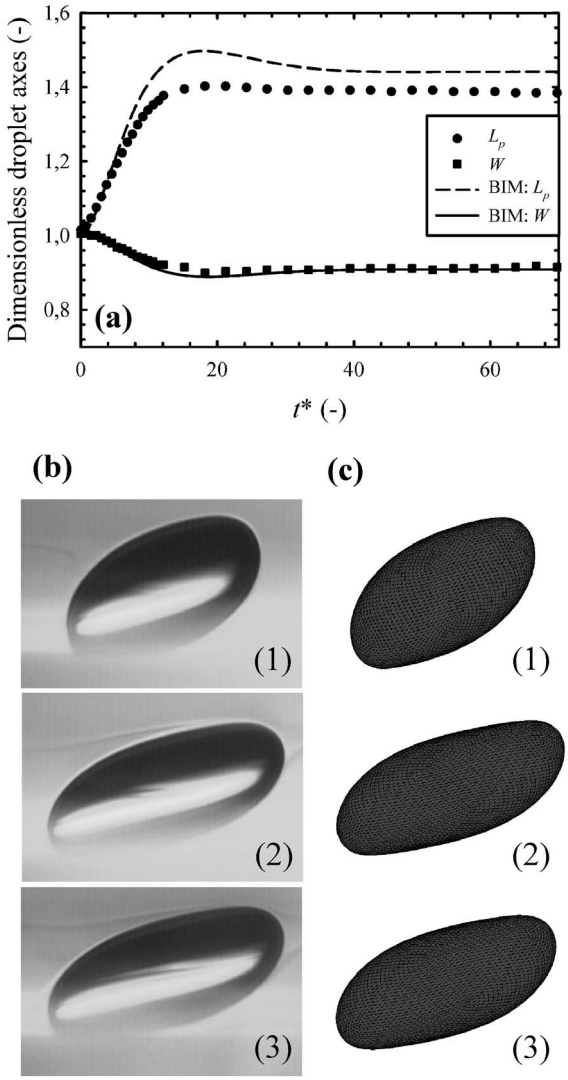


FIG. 10. Startup data at Ca=0.2 for $2R/d=0.88$. (a) Comparison between experimental and numerical droplet dimensions as a function of dimensionless time. (b) Experimental droplet shape and (c) numerical droplet shape at $t^*=$(1) 5.1, (2) 21.1, and (3) 60.6.

The results in Figs. 9–11 show transient dynamics during startup at conditions relatively far from critical. In Fig. 12, however, the droplet dimensions are shown as a function of time for the same confined droplet ($2R/d=0.88$) as in Fig. 11, but this time at a near-critical capillary number of 0.4. As can be seen in Fig. 12, both the experimental results and the predictions of the numerical model show again a large overshoot in $L_p$. Under the present conditions, the simulations predict a damped oscillatory behavior, as was also observed by Renardy.[22] The experimental maximum occurs a little bit earlier in time compared to the numerical maximum, and since the experiment is stopped earlier, no conclusions of damped oscillatory behavior can be drawn here. However, similar experiments performed by Sibillo *et al.* did show these damped oscillations.[19]

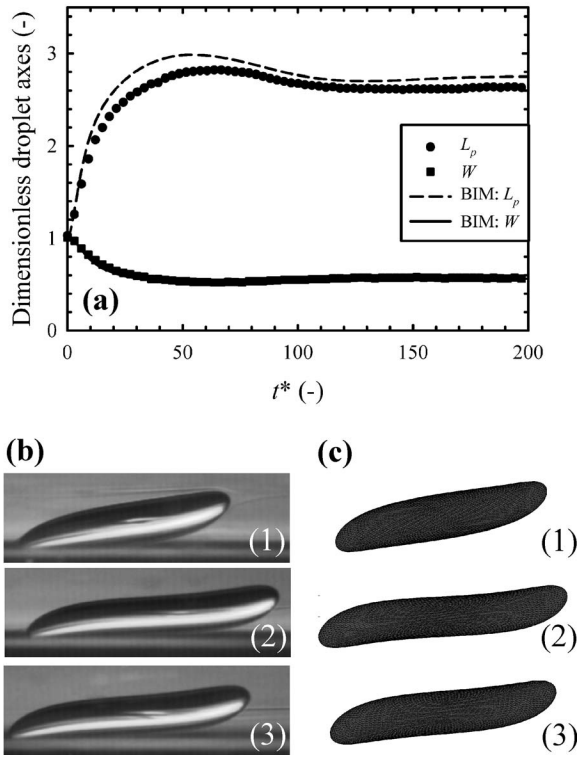


FIG. 11. Startup data at Ca=0.35 for $2R/d$=0.88. (a) Comparison between experimental and numerical droplet dimensions as a function of dimensionless time. (b) Experimental droplet shape and (c) numerical droplet shape at $t^*$=(1) 18.2, (2) 60.6, and (3) 135.5.

Under all conditions of transient behavior shown here, it can be stated that, at a viscosity ratio of unity, the numerical model is capable of predicting an increased transient deformation of confined droplet with respect to bulk droplets and a correct droplet shape when compared to the experimental results. However, the model predicts a slightly higher deformation than experimentally observed.

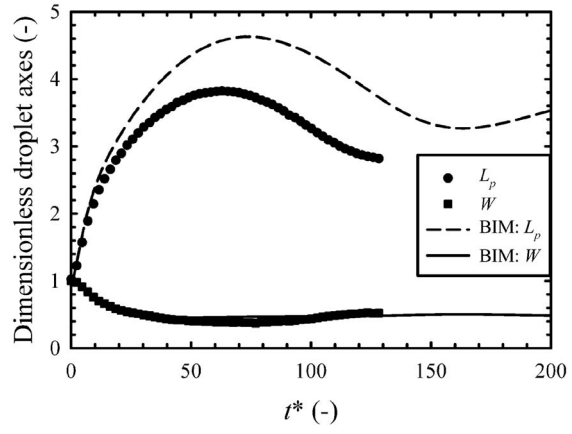


FIG. 12. Startup data at Ca=0.4 for $2R/d$=0.88: Comparison between experimental and numerical droplet dimensions as a function of dimensionless time.

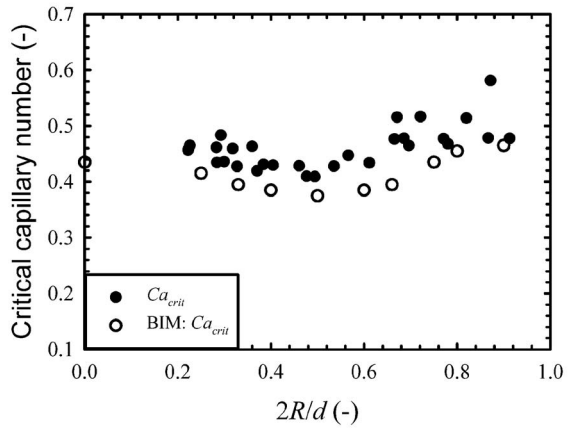


FIG. 13. Experimental and numerical critical capillary number as a function of confinement ratio for λ=1.

### C. Breakup

Since some quantitative differences in deformation are seen at near-critical capillary numbers, also a comparison between the experimentally obtained critical capillary number and the numerically calculated one is made as a function of degree of confinement (Fig. 13). All computations started with initially spherical drops and the simulations were run until a stationary state was reached, or until the drop broke up. The critical capillary number was determined within 0.01. It is seen in Fig. 13 that the critical capillary number decreases slightly with increasing confinement ratio until a minimum is reached around a degree of confinement of 0.5. A further increase in confinement ratio causes $Ca_{crit}$ to increase again to a value slightly higher than the unconfined result. Good agreement is seen between the experimental and the numerical results. However, the numerical results are systematically lower than the experimental ones. The numerical value, however, is determined at the capillary number in between the last steady-state value and the first breakup value at an accuracy of 0.01. On the other hand, the experimental results, which indicate the capillary number at which breakup is first seen, are less precisely determined, and hence a small overestimation of the real critical capillary number is made. Unlike confined breakup results at viscosity ratios $\neq 1$, at a viscosity ratio of 1, little effect of confinement on the critical value is seen, both numerically and experimentally.

## V. CONCLUSIONS

The dynamics of single droplets confined between two parallel plates is investigated both numerically and experimentally. A boundary integral method, in which the Green's functions were modified to include wall effects, is used here. The numerical results are validated with experimental data obtained in a counter-rotating parallel plate device. The droplet shape, deformation, and orientation in shear flow are studied as a function of capillary number and confinement ratio for a viscosity ratio of unity. It was first shown that the results of the modified BIM model match the experimental results of unconfined droplets during startup and steady-state

shear flow. Therefore, it can be concluded that the model is capable of predicting the dynamics of droplets in the limiting case of an unbounded flow field. However, droplets that are confined between two parallel plates show clearly a different behavior compared to bulk droplets. It was seen that confinement induces a sigmoidal droplet shape during shear flow. Contrary to other models, the modified BIM model is capable of predicting the right droplet shape at any point in time. The model also predicts an increase in deformation and more orientation toward the flow direction as a function of confinement ratio, which could all be experimentally confirmed. Velocity and pressure profiles have been calculated. Whereas the velocity profiles both inside and outside the droplet are not affected significantly by the degree of confinement, the pressure profile outside a confined droplet is observed to be drastically different. Upon startup of flow, both the experimental data and the numerical results show oscillatory behavior for highly confined droplets. This behavior is characterized by one or more overshoots in droplet length followed by droplet retraction toward a sigmoidal, largely deformed steady-state shape. Again, good agreement was seen between the experimental and the numerical data, when comparing the shape and magnitude of deformation. However, the numerical model systematically predicted a larger deformation with respect to the experimental results for highly confined and highly deformed droplets, especially at near-critical conditions. However, despite these differences in deformation, it has been shown that the numerical model and the experimental results display the same behavior with respect to the critical capillary number.

## ACKNOWLEDGMENTS

Anja Vananroye thanks the FWO Vlaanderen (Project No. G.0523.04) and Onderzoeksfonds K.U. Leuven (Grant No. GOA 03/06) for financial support. Pieter J. A. Janssen acknowledges support by the Dutch Polymer Institute (DPI) (Project No. 446).

[1] H. P. Grace, "Dispersion phenomena in high viscosity immiscible fluid systems and application of static mixers as dispersion devices in such systems," Chem. Eng. Commun. **14**, 225 (1982).
[2] G. I. Taylor, "The viscosity of a fluid containing small drops of another fluid," Proc. R. Soc. London, Ser. A **138**, 41 (1932).
[3] J. M. Rallison, "The deformation of small viscous drops and bubbles in shear flows," Annu. Rev. Fluid Mech. **16**, 45 (1984).
[4] H. A. Stone, "Dynamics of drop deformation and breakup in viscous fluids," Annu. Rev. Fluid Mech. **26**, 65 (1994).
[5] C. L. Tucker and P. Moldenaers, "Microstructural evolution in polymer blends," Annu. Rev. Fluid Mech. **34**, 177 (2002).
[6] S. Guido and F. Greco, "Dynamics of a liquid drop in a flowing immiscible liquid," in *Rheology Reviews*, edited by D. M. Binding and K. Walters (British Society of Rheology, Aberystwyth, UK, 2004), pp. 99–142.
[7] H. A. Stone, A. D. Stroock, and A. Ajdari, "Engineering flows in small devices: Microfluidics toward a lab-on-a-chip," Annu. Rev. Fluid Mech. **36**, 381 (2004).
[8] T. M. Squires and S. R. Quake, "Microfluidics: Fluid physics at the nanoliter scale," Rev. Mod. Phys. **77**, 977 (2005).
[9] T. Thorsen, R. W. Roberts, F. H. Arnolds, and S. R. Quake, "Dynamic pattern formation in a vesicle-generating microfluidic device," Phys. Rev. Lett. **86**, 4163 (2001).
[10] J. D. Tice, A. D. Lyon, and R. F. Ismagilov, "Effects of viscosity on droplet formation and mixing in microfluidic channels," Anal. Chim. Acta **507**, 73 (2004).
[11] P. Garstecki, H. A. Stone, and G. M. Whitesides, "Mechanism for flow-rate controlled breakup in confined geometries: A route to monodisperse emulsions," Phys. Rev. Lett. **94**, 164501 (2005).
[12] P. Garstecki, M. J. Fuerstman, H. A. Stone, and G. M. Whitesides, "Formation of droplets and bubbles in a microfluidic T-junction—Scaling and mechanism of break-up," Lab Chip **6**, 437 (2006).
[13] A. Vananroye, P. Van Puyvelde, and P. Moldenaers, "Morphology development during microconfined flow of viscous emulsions," Appl. Rheol. **16**, 242 (2006).
[14] K. B. Migler, "String formation in sheared polymer blends: Coalescence, breakup and finite size effects," Phys. Rev. Lett. **86**, 1023 (2001).
[15] J. A. Pathak, M. C. Davis, S. D. Hudson, and K. B. Migler, "Layered droplet microstructures in sheared emulsions: Finite-size effects," J. Colloid Interface Sci. **255**, 391 (2002).
[16] J. A. Pathak and K. B. Migler, "Droplet-string deformation and stability during microconfined shear flow," Langmuir **19**, 8667 (2003).
[17] A. Vananroye, P. Van Puyvelde, and P. Moldenaers, "Structure development in confined polymer blends: Steady-state shear flow and relaxation," Langmuir **22**, 2273 (2006).
[18] A. Vananroye, P. Van Puyvelde, and P. Moldenaers, "Effect of confinement on droplet breakup in sheared emulsions," Langmuir **22**, 3972 (2006).
[19] V. Sibillo, G. Pasquariello, M. Simeone, V. Cristini, and S. Guido, "Drop deformation in microconfined shear flow," Phys. Rev. Lett. **97**, 054502 (2006).
[20] A. Vananroye, P. Van Puyvelde, and P. Moldenaers, "Effect of confinement on the steady-state behavior of single droplets during shear flow," J. Rheol. **51**, 139 (2007).
[21] M. Shapira and S. Haber, "Low Reynolds number motion of a droplet in shear flow including wall effects," Int. J. Multiphase Flow **16**, 305 (1990).
[22] Y. Renardy, "The effects of confinement and inertia on the production of droplets," Rheol. Acta **46**, 521 (2007).
[23] P. J. A. Janssen and P. D. Anderson, "Boundary integral method for drop deformation between parallel plates," Phys. Fluids **19**, 043602 (2007).
[24] A. J. Griggs, A. Z. Zinchenko, and R. H. Davis, "Low-Reynolds-number motion of a deformable drop between two parallel plane walls," Int. J. Multiphase Flow **33**, 182 (2007).
[25] R. B. Jones, "Spherical particle in Poiseuille flow between planar walls," J. Chem. Phys. **121**, 483 (2004).
[26] N. Liron and S. Mochon, "Stokes flow for a Stokeslet between 2 parallel flat plates," J. Eng. Math. **10**, 287 (1976).
[27] J. M. Rallison and A. Acrivos, "A numerical study of the deformation and burst of a viscous drop in an extensional flow," J. Fluid Mech. **89**, 191 (1978).
[28] C. Pozrikidis, *Boundary-Integral and Singularity Methods for Linearized Viscous Flow* (Cambridge University Press, Cambridge, UK, 1992).
[29] M. Rother, A. Zinchenko, and R. Davis, "Buoyancy-driven coalescence of slightly deformable drops," J. Fluid Mech. **346**, 117 (1997).
[30] A. Zinchenko, M. Rother, and R. Davis, "A novel boundary-integral algorithm for viscous interaction of deformable drops," Phys. Fluids **9**, 1493 (1997).
[31] V. Cristini, J. Blawzdziewicz, and M. Loewenberg, "Drop breakup in three-dimensional viscous flows," Phys. Fluids **10**, 1781 (1998).
[32] S. Yon and C. Pozrikidis, "A finite-volume/boundary-element method for flow past interfaces in the presence of surfactants, with application to shear flow past a viscous drop," Comput. Fluids **27**, 879 (1998).
[33] C. D. Eggleton, Y. P. Pawar, and K. J. Stebe, "Insoluble surfactants on a drop in an extensional flow: A generalization of the stagnated surface limit to deforming interfaces," J. Fluid Mech. **385**, 79 (1999).
[34] M. E. Staben, A. Z. Zinchenko, and R. H. Davis, "Motion of a particle between two parallel plane walls in low-Reynolds-number Poiseuille flow," Phys. Fluids **15**, 1711 (2003).
[35] M. E. Staben, K. P. Galvin, and R. H. Davis, "Low-Reynolds-number motion of a heavy sphere between two parallel plane walls," Chem. Eng. Sci. **61**, 1932 (2006).
[36] M. E. Staben, A. Z. Zinchenko, and R. H. Davis, "Dynamic simulation of spheroid motion between two parallel plane walls in low-Reynolds-number Poiseuille flow," J. Fluid Mech. **553**, 187 (2006).
[37] I. Bazhlekov, P. D. Anderson, and H. E. H. Meijer, "Non-singular boundary-integral method for deformable drops in viscous flows," Phys. Fluids **16**, 1064 (2004).
[38] M. Loewenberg and E. Hinch, "Numerical simulation of concentrated

emulsion in shear flow," J. Fluid Mech. **321**, 395 (1996).
[39]I. Vinckier, P. Moldenaers, and J. Mewis, "Relationship between rheology and morphology of model blends in steady shear flow," J. Rheol. **40**, 613 (1996).
[40]I. Sigillo, L. di Santo, S. Guido, and N. Grizzuti, "Comparative measurements of interfacial tension in a model polymer blend," Polym. Eng. Sci. **37**, 1540 (1997).
[41]M. Minale, P. Moldenaers, and J. Mewis, "Effect of shear history on the morphology of immiscible polymer blends," Macromolecules **30**, 5470 (1997).